The Astrophysical Journal, 680:764–773, 2008 June 10

CENTER-TO-LIMB VARIATION OF SOLAR THREE-DIMENSIONAL HYDRODYNAMICAL SIMULATIONS

L. Koesterke, C. Allende Prieto,[1] and D. L. Lambert
McDonald Observatory and Department of Astronomy, University of Texas, Austin, TX 78712
Received 2007 September 11; accepted 2008 February 12

ABSTRACT

We examine closely the solar center-to-limb variation of continua and lines and compare observations with predictions from both a three-dimensional (3D) hydrodynamic simulation of the solar surface (provided by M. Asplund and collaborators) and one-dimensional (1D) model atmospheres. Intensities from the 3D time series are derived by means of the new synthesis code ASSϵT, which overcomes limitations of previously available codes by including a consistent treatment of scattering and allowing for arbitrarily complex line and continuum opacities. In the continuum, we find very similar discrepancies between synthesis and observation for both types of model atmospheres. This is in contrast to previous studies that used a ''horizontal'' and time-averaged representation of the 3D model and found a significantly larger disagreement with observations. The presence of temperature and velocity fields in the 3D simulation provides a significant advantage when it comes to reproducing solar spectral line shapes. Nonetheless, a comparison of observed and synthetic equivalent widths reveals that the 3D model also predicts more uniform abundances as a function of position angle on the disk. We conclude that the 3D simulation provides not only a more realistic description of the gas dynamics, but despite its simplified treatment of the radiation transport, it also predicts reasonably well the observed center-to-limb variation, which is indicative of a thermal structure free from significant systematic errors.

Subject headings: hydrodynamics — line: formation — radiative transfer — Sun: abundances — Sun: photosphere

1. INTRODUCTION

A few years back, it was realized that one of the most ''trusted'' absorption lines to gauge the oxygen abundance in the solar photosphere, the forbidden [O I] line at 6300 Å, was blended with a Ni I transition. These two transitions overlap so closely that only a minor distortion is apparent in the observed feature. Disentangling the two contributions with the help of a three-dimensional (3D) hydrodynamical simulation of surface convection led us to propose a reduction of the solar photospheric abundance by $\sim$30% (Allende Prieto et al. 2001). Using the same solar model, subsequent analysis of other atomic oxygen and OH lines confirmed the lower abundance, resulting in an average value of $\log \epsilon_{\rm O} = 8.66 \pm 0.05$ (Asplund et al. 2004).[2]

This reduction in the solar O/H ratio, together with a parallel downward revision for carbon (Allende Prieto et al. 2002; Asplund et al. 2005b), ruins the nearly perfect agreement between models of the solar interior and seismological observations (Bahcall et al. 2005; Delahaye & Pinsonneault 2006; Lin et al. 2007). A brief overview of the proposed solutions is given by Allende Prieto (2008). Interior and surface models appear to describe two different stars.

Supporters of the new hydrodynamical models, and the revised surface abundances, focus on their strengths: they include more realistic physics and are able to reproduce extremely well detailed observations (oscillations, spectral line asymmetries and net wavelength blueshifts, granulation contrast and topology). Detractors emphasize the fact that the new models necessarily employ a simplified description of the radiation field and have not been tested to the same extent as classical one-dimensional (1D) models. The calculation of spectra for 3D time-dependent models is a demanding task, which is likely the main reason why some fundamental tests have not yet been performed for the new models.

On the basis of 1D radiative transfer calculations, Ayres et al. (2006) suggest that the thermal profile of the solar surface convection simulation of Asplund et al. (2000) may be incorrect. Ayres et al. (2006) make use of a 1D average, both ''horizontal'' and over time, of the 3D simulation to analyze the center-to-limb variation in the continuum, finding that the averaged model performs much more poorly than the semiempirical FAL C model of Fontenla et al. (1993). When the FAL C model is adopted, Ayres et al. (2006) find that an analysis of CO lines leads to a much higher oxygen abundance, and therefore they question the downward revision proposed earlier. Note, in contrast, that Fontenla et al. (2007) favor the lower C and O abundances when using the most recent reincarnation (SRPM 305) of their detailed semiemperical model.

Allende Prieto et al. (2008) argues that when classical 1D model atmospheres are employed, the inferred oxygen abundance from atomic features differs by only 0.05 dex between an analysis in 1D and 3D. The difference is even smaller for atomic carbon lines. When the hydrodynamical model is considered, there is good agreement between the oxygen abundance inferred from atomic lines and from OH transitions (Asplund et al. 2004; Scott et al. 2006). A high value of the oxygen abundance is derived only when considering molecular tracers in 1D atmospheres, perhaps not a surprising result given the high sensitivity to temperature of the molecular dissociation. A low oxygen abundance ($\log \epsilon_{\rm O} = 8.63$) value is also deduced from atomic lines and atmospheric models based on the inversion of spatially resolved polarimetric data (Socas-Navarro & Norton 2007).

Despite the balance seeming favorable to the 3D models and the low values of the oxygen and carbon abundances, a failure of the 3D model to match the observed limb darkening, as suggested by the experiments of Ayres et al. (2006), would be reason for serious concern. In the present paper, we perform spectral synthesis on the solar surface convection simulation of Asplund

[1] Current address: Mullard Space Science Laboratory, University College London, Holmbury St. Mary, Surrey RH5 6NT, UK.
[2] Here $\epsilon_{\rm X} = N_{\rm X}/N_{\rm H} \times 10^{12}$.

et al. (2000) with the goal of testing its ability to reproduce the observed center-to-limb variations of both the continuum intensities and the equivalent widths of spectral lines. We compare its performance with commonly used theoretical 1D model atmospheres. Our calculations are rigorous; they take into account the four-dimensionality of the hydrodynamical simulation: its 3D geometry and time dependency. After a concise description of our calculations in § 2, § 3 outlines the comparison with solar observations and § 4 summarizes our conclusions.

2. MODELS AND SPECTRUM SYNTHESIS

We investigate the center-to-limb variation (CLV) of the solar spectrum for the continuum and lines. Snapshots taken from 3D hydrodynamical simulations of the solar surface by Asplund et al. (2000) serve as model atmospheres. The synthetic continuum intensities and line profiles are calculated by means of the new spectrum synthesis code ASSϵT (Advanced Spectrum Synthesis 3D Tool), which is designed to solve accurately the equation of radiation transfer in 3D. The new synthesis code will be described in detail by L. Koesterke et al. (in preparation), and only the key features are highlighted in subsequent sections.

2.1. *Hydrodynamic Models*

The simulation of solar granulation was carried out with a 3D, time-dependent, compressible, radiative hydrodynamics code (Nordlund & Stein 1990; Stein & Nordlund 1989; Asplund et al. 1999). The simulation describes a volume of $6.0 \times 6.0 \times 3.8$ Mm (about 1 Mm being above $\tau_{\rm cont} \approx 1$) with $200 \times 200 \times 82$ equidistantly spaced grid points over 2 hr of solar time. About 10 granules are included in the computed domain at any given time.

Ninety-nine snapshots were taken in 30 s intervals from a shorter sequence of 50 minutes. The grid points and the physical dimensions are changed to accommodate the spectrum synthesis: The horizontal sampling is reduced by omitting three out of four grid points in both directions; the vertical extension is decreased by omitting layers below $\tau_{\rm cont}^{\rm min} \approx 300$ while keeping the number of grid points in the z-direction constant, i.e., by increasing the vertical sampling and introducing a nonequidistant vertical grid. After these changes, a single snapshot covers approximately a volume of $6.0 \times 6.0 \times 1.7$ Mm with $50 \times 50 \times 82$ grid points (Asplund et al. 2000).

2.2. *Spectrum Synthesis*

Compared to the spectrum synthesis in one dimension, the calculation of emergent fluxes and intensities from 3D snapshots is a tremendous task, even when LTE is applied. Previous investigations (e.g., Asplund et al. 2000; Ludwig & Steffen 2008) were limited to the calculation of a single line profile or a blend of very few individual lines on top of constant background opacities, and without scattering. In order to overcome these limitations, we devise a new scheme that is capable of dealing with arbitrary line blends, frequency-dependent continuum opacities, and scattering. The spectrum synthesis is divided into five separate tasks that are outlined below. A more detailed description which contains all essential numerical tests will be given by L. Koesterke et al. (in preparation).

2.2.1. *Opacity Interpolation*

For the 3D calculations we face a situation in which we have to provide detailed opacities for $\approx 2 \times 10^7$ grid points for every single frequency under consideration. Under the assumption of LTE, the size of the problem can be reduced substantially by using an interpolation scheme to derive opacities from a data set that has orders of magnitude fewer data points. We introduce an *opacity* grid that covers all grid points of the snapshots in the temperature-density plane. The grid points are regularly spaced in $\log T$ and $\log \rho$ with typical intervals of 0.018 and 0.25 dex, respectively.

We use piecewise cubic Bezier polynomials that do not introduce artificial extrema (Auer 2003). To enable third-order interpolations close to the edges, additional points are added to the opacity grid. The estimated interpolation error is well below 0.1% for the setup used throughout the present paper.

2.2.2. *Opacity Calculation*

We use a modified version of SYNSPEC (Hubeny & Lanz 1995) to prepare frequency-dependent opacities for the relatively small numbers of grid points in the opacity grid. The modifications allow for the calculation of opacities on equidistant $\log \lambda$ scales, to output the opacities to binary files, and to skip the calculation of intensities.

Two data sets are produced. Continuum opacities are calculated at intervals of about 1 Å at 3000 Å. Full opacities (continuum and lines) are provided at a much finer spacing of $0.3 v_{\rm min}$, where $v_{\rm min}$ is the thermal velocity of an iron atom at the minimum temperature of all grid points in all snapshots under consideration. A typical step in wavelength is 2.7×10^{-3} Å at 3000 Å, which corresponds to 0.27 km s^{-1}.

We adopt the solar photospheric abundances recently proposed by Asplund et al. (2005a) with carbon and oxygen abundances of $\log \epsilon = 8.39$ and 8.66, respectively, which are about 30% less than in earlier compilations (Grevesse & Sauval 1998). We account for bound-bound and bound-free opacities from hydrogen and from the first two ionization stages of He, C, N, O, Na, Mg, Al, Si, Ca, and Fe. Bound-free cross sections for all metals but iron are taken from TOPBASE and smoothed as described by Allende Prieto et al. (2003). Iron bound-free opacities are derived from the photoionization cross sections computed by the Iron Project (see, e.g., Nahar 1995; Bautista 1997), after smoothing.

Bound-bound $\log(gf)$ values are taken from Kurucz, augmented by damping constants from Barklem et al. (2000) where available. We also account for bound-free opacities from H^-, H_2^+, CH, and OH, and for a few million molecular lines from the nine most prominent molecules in the wavelength range from 2200 to 7200 Å. Thomson and Rayleigh (atomic hydrogen) scattering are considered as well, as described below in § 2.2.3. The equation of state is solved considering the first 99 elements and 338 molecular species. Chemical equilibrium is assumed for the calculation of the molecular abundances, and the atomic abundances are updated accordingly (I. Hubeny, private communication).

2.2.3. *Scattering*

We employ a background approximation, calculating the radiation field J_ν for the sparse continuum frequency points for which we have calculated the continuum opacity without any contribution from spectral lines. The calculation starts at the bluemost frequency, and the velocity field is neglected at this point: no frequency coupling is present. The opacities for individual grid points are derived by interpolation from the opacity grid, and the emissivities are calculated assuming LTE. As mentioned above, we include electron (Thomson) scattering and Rayleigh scattering by atomic hydrogen. An accelerated lambda iteration (ALI) scheme is used to obtain a consistent solution of the mean radiation field J_ν and the source function S_ν at all grid points. In turn, J_ν is calculated from S_ν and vice versa, accelerating the iteration by amplifying $\Delta J_\nu = J_\nu^{\rm New} - J_\nu^{\rm Old}$ by the factor $1/(1 - \Lambda^*)$, where Λ^* is the approximate lambda operator (Olson & Kunasz 1987). Generally the mean radiation from the last frequency point, i.e., the

frequency to the blue, serves as an initial guess of J_ν at the actual frequency. At the first frequency point, the iteration starts with $J_\nu = S_\nu$.

The formal solution, i.e., the solution of the equation $J_\nu = \Lambda S_\nu$, is obtained by means of a short characteristics scheme (Olson & Kunasz 1987). For all grid points the angle-dependent intensity I_ν^μ is derived by integrating the source function along the ray between the grid point itself and the closest intersection of the ray with a horizontal or vertical plane in the mesh. The operator Λ^* needed for the acceleration is calculated within the formal solution.

For the present calculations, J_ν is integrated from I_ν^μ at 48 angles (six in μ, eight in ϕ). The integration in μ is performed by a three-point Gaussian quadrature for each half-space, i.e., for rays pointing to the outer and the inner boundary, respectively. The integration in ϕ is trapezoidal. The opacities and source functions are assumed to vary linearly (first-order scheme) along the ray.

In order to integrate the intensity between the grid point and the point of intersection where the ray leaves the grid cell, the opacity, the source function, and the specific intensity (κ_ν, S_ν, and I_ν^μ, respectively) have to be provided at both ends of the ray. Since the point where the ray leaves the cell is generally not a grid point itself, an interpolation scheme has to be employed to derive the required quantities. We perform interpolations in two dimensions on the surfaces of the cuboids applying again Bezier polynomials with control values that avoid the introduction of artificial extrema. The interpolation may be a source of significant numerical inaccuracies. Detailed tests, using an artificial 3D structure constructed by horizontally replicating a 1D model, revealed that a third-order interpolation scheme provides sufficient accuracy where linear interpolations fail in reproducing the radiation field: the mean relative errors are 0.5% and 0.05% for linear and cubic interpolation, respectively.

It is possible, in terms of computing time, to calculate J_ν from the full opacity data set for all frequencies (our "fine" sampling). However, since the total effect of scattering for the solar case in the optical is quite small, the differences between the two methods are negligible. Therefore, we apply the faster method throughout this paper. Note that in both approximations (using background or full opacities), the calculation of the mean radiation field does not account for any frequency coupling.

2.2.4. *Calculation of Intensities and Fluxes*

The emergent flux is calculated from the opacities of the full data set provided at the fine frequency grid. Again, the opacities for individual grid points are derived by interpolation from the opacity grid, and the emissivities are calculated from LTE. The mean background radiation field J_ν is interpolated from the coarser continuum frequency grid to the actual frequency, and it contributes to the source function at all grid points via Thomson and Rayleigh (atomic hydrogen) scattering opacities.

The integration along a ray is performed in the observer's frame by following long characteristics from the top layer down to optical depths of $\tau_{\rm Ray} > 20$. Frequency shifts due to the velocity field are applied to the opacities and source functions. Each ray starts at a grid point of the top layer and is built by the points of intersection of the ray and the mesh. At these points of intersection an interpolation in three dimensions is generally performed; i.e., a two-dimensional (2D) geometric interpolation in the *X-Y*, *X-Z*, or *Y-Z* plane, respectively, is enhanced by an interpolation in frequency necessitated by the presence of the velocity field. Additional points are inserted into the ray to ensure full frequency coverage of the opacities. This is done when the difference of the velocity field projected onto the ray between the entry and exit point of a grid cell exceeds the frequency spacing of the opacity. Without these additional points and in the presence of large velocity gradients, line opacities could be underestimated along the ray—a line could be shifted to one side at the entry point and to the other side at the exit point—leaving only neighboring continuum opacities visible to both points while the line is hidden within the cell.

Similar to the calculation of the mean radiation field J described in § 2.2.3, all interpolations in both space and frequency are based on piecewise cubic Bezier polynomials. It is not completely trivial to mention that for the accurate calculation of the emergent intensities, the application of a high-order interpolation scheme is much more important than it is for the calculation of the mean background radiation field (§ 2.2.3). Here we are calculating precisely the quantity we are interested in, i.e., specific intensities. But in addition to that, we deal with interpolations in three dimensions (two in space, one in frequency) instead of a 2D interpolation in space. Hence, any quantity is derived from 21 1D interpolations rather than just five.

In the standard setup of the 3D calculations, 20 rays are used for the integration of the flux F_ν from the intensities I_ν^μ. Similar to the integration of J described in § 2.2.3, the integration in μ is a three-point Gaussian quadrature, while the integration in ϕ is trapezoidal. Eight angles in ϕ are assigned to the first two of the μ angles while the last and most inclined angle with the by far smallest (flux) integration weight has four contributing ϕ angles. Note that for the investigation of the center-to-limb variation, the number of angles and their distribution in μ and ϕ differs considerably from this standard setup, as explained below (§ 3.1).

2.3. *Spectra in One Dimension*

To facilitate consistent comparisons of spectra from 3D *and* 1D models, the new spectrum synthesis code ASSϵT also accepts 1D structures as input. Consistency is achieved by the use of the same opacity data (see § 2.2.2) and its interpolation (if desired in 1D, see § 2.2.1) and by the application of the same radiation transfer solvers, i.e., first-order short- and long-characteristic schemes (see §§ 2.2.3 and 2.2.4, respectively). All angle integrations are performed by means of a three-point Gaussian formula. This leaves the interpolations inherent to the radiation transfer scheme in 3D as the only major inconsistency between the spectra in 1D and 3D. Numerical tests have revealed that these remaining inconsistencies are quite small, as we will report in an upcoming paper.

2.4. *Solar Model*

Our choice is not to use a semiempirical model of the solar atmosphere as a 1D comparison with the 3D hydrodynamical simulation, but a theoretical model atmosphere. Semiempirical models take advantage of observations to constrain the atmospheric structure, a fact that would constitute an unfair advantage over the 3D simulation. Some semiempirical models, in particular, use observed limb darkening curves, and of course it is meaningless to test their ability to reproduce the same or different observations of the center-to-limb variation in the continuum. Consequently we are using models from Kurucz, the MARCS group, and a horizontal- and time-averaged representation of the 3D hydrodynamical simulations.

We have derived a 1D solar reference model from the Kurucz grid (Kurucz 1993). The reference model is derived from third-order interpolations in τ, $T_{\rm eff}$, $\log g$, and Z. Details of the interpolation scheme will be presented elsewhere. We have adopted the usual values of $T_{\rm eff} = 5777$ K and $\log g = 4.437$ (cgs) but a

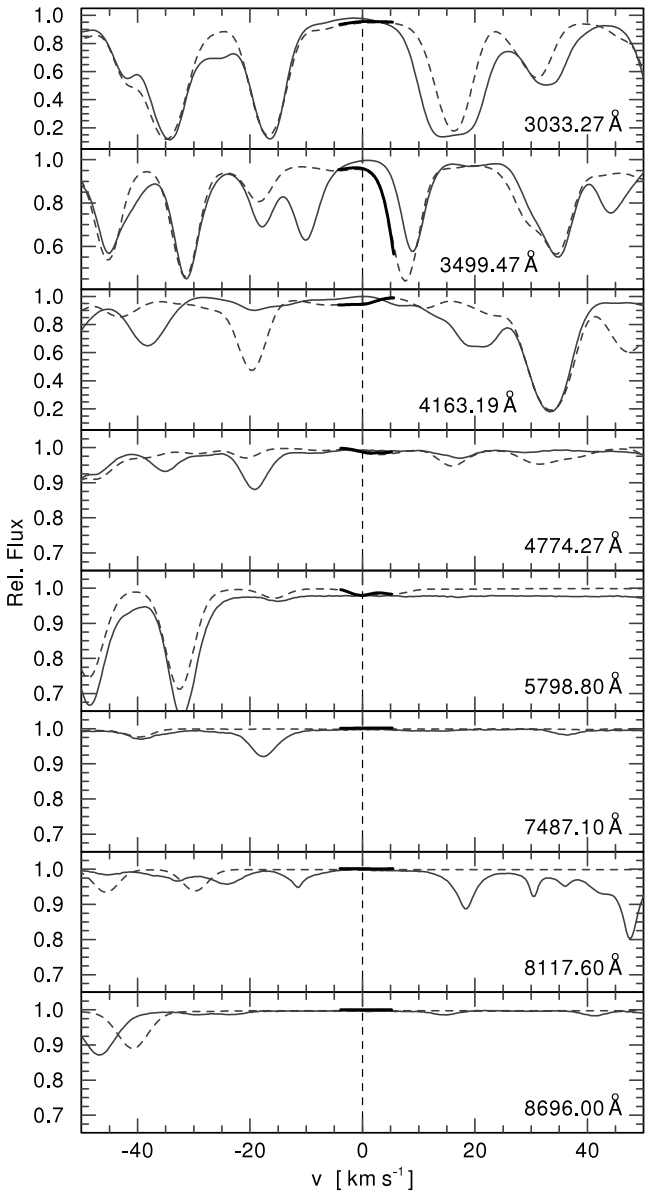

FIG. 1.—Comparison of the normalized solar spectrum (*thin solid lines*), the synthetic spectra from the 1D Kurucz model (*dashed lines*) and the 3D hydrosimulation (*thick solid lines*) for the eight wavelengths under consideration. The 3D calculations were performed only for the small windows of ± 5 km s^{-1} used here to study the center-to-limb variation in the continuum. For the normalization, the synthetic spectra were divided by the corresponding "pure continuum" spectra. The 1D spectrum has been convolved with a Gaussian of FWHM = 4.3 km s^{-1}, to account for macroturbulence (FWHM = 4.2 km s^{-1}) and the finite resolution of the solar atlas (FWHM = 0.8 km s^{-1}). Note that the $\log(gf)$ values of the individual lines have not been adjusted to match the spectrum.

reduced metallicity of $\log(Z/Z_\odot) = -0.2$ in an attempt to account globally for the difference between the solar abundances (mainly iron) used in the calculation of the model and more recent values, as described by Allende Prieto et al. (2006). To avoid a biased result by using a single 1D comparison model, we have also experimented with a solar MARCS model kindly provided by M. Asplund, and a solar model interpolated from the more recent ODFNEW grid from Kurucz.[3] No metallicity correction was applied to these newer solar models.

In earlier investigations (Ayres et al. 2006), a 1D representation (Asplund et al. 2005b) of the 3D time series, i.e., a "horizontal" average[4] over time, was used to study the thermal profile of the 3D model. While this approximation allows easy handling by means of a 1D radiation transfer code, the validity of this approach has never been established. In order to investigate the limitations of this shortcut, we compare its center-to-limb variation in the continuum with the exact result from the 3D radiation transfer on the full series of snapshots.

3. CENTER-TO-LIMB VARIATION

3.1. *Continuum*

Neckel & Labs (1994) and Neckel (2003, 2005) investigated the center-to-limb variation of the Sun based on observations taken at the National Solar Observatory (Kitt Peak) in 1986 and 1987. They describe the observed intensities across the solar disk as a function of the heliocentric distance by fifth-order polynomials for 30 frequencies between 303 and 1099 nm. Similar observations by Petro et al. (1984) and Elste & Gilliam (2007; with a smaller spectral coverage) indicate that Neckel & Labs (1994) may have overcorrected for scattered light, but confirm a level of accuracy of $\approx$0.4%. We have calculated fluxes and intensities for small spectral regions (± 5 km s^{-1}) around eight frequencies (corresponding to standard air wavelengths of 3033.27, 3499.47, 4163.19, 4774.27, 5798.80, 7487.10, 8117.60, and 8696.00 Å) and compare monochromatic synthetic intensities with the data from Neckel & Labs (1994). Because the spectral regions are essentially free from absorption lines, the width of the bandpass of the observations varying between 1.5 km s^{-1} in the blue (3030 Å) and 1.9 km s^{-1} in the red (10990 Å) is irrelevant.

The fluxes were integrated from 20 and 3 angles (see §§ 2.2.4 and 2.3) for the 3D and 1D calculations, respectively. For the study of the CLV, intensities were calculated for 11 positions on the Sun ($\mu \equiv \cos\theta = 1.0, 0.9, \ldots, 0.1, 0.05$) averaging over four directions in ϕ and all horizontal X-Y positions. All 99 snapshots were utilized for the 3D calculations.

The eight frequencies cover a broad spectral range. Although some neighboring features are poorly matched by our synthetic spectra, the solar flux spectrum of Kurucz et al. (1984) is reproduced well at the frequencies selected by Neckel & Labs, and therefore modifications of our line list were deemed unnecessary (see Fig. 1). The normalization of the synthetic spectra was achieved by means of "pure continuum" fluxes that were derived from calculations lacking all atomic and molecular line opacities—Figure 1 shows that Neckel & Labs did a superb job selecting continuum windows.

Comparisons of observed and synthetic CLVs are conducted with data sets that are normalized with respect to the intensity at the disk center; i.e., all intensities are divided by the central intensity. We show the residual CLVs,

$$\mathrm{RCLV} \equiv I_\mu^{\mathrm{obs}}/I_{\mu=1}^{\mathrm{obs}} - I_\mu^{\mathrm{syn}}/I_{\mu=1}^{\mathrm{syn}}, \quad (1)$$

in Figure 2. The RCLVs within each group are quite homogeneous. In addition to the data derived from our 1D Kurucz model (see § 2.4), we show also data from two other 1D models, i.e., a MARCS model (*first panel*) from M. Asplund (private communication) and an alternative (ODFNEW) Kurucz model (*second panel*) from a different model grid.[5] The center-to-limb variations from both alternatives show much larger residuals and are not used for the comparison with the 3D data. However, the scatter

[3] Available on his Web site at http://kurucz.harvard.edu.

[4] "Horizontal average," in this context, refers to the mean value over a surface with constant vertical optical depth, rather than over a constant geometrical depth.

[5] See http://kurucz.harvard.edu/grids.html.

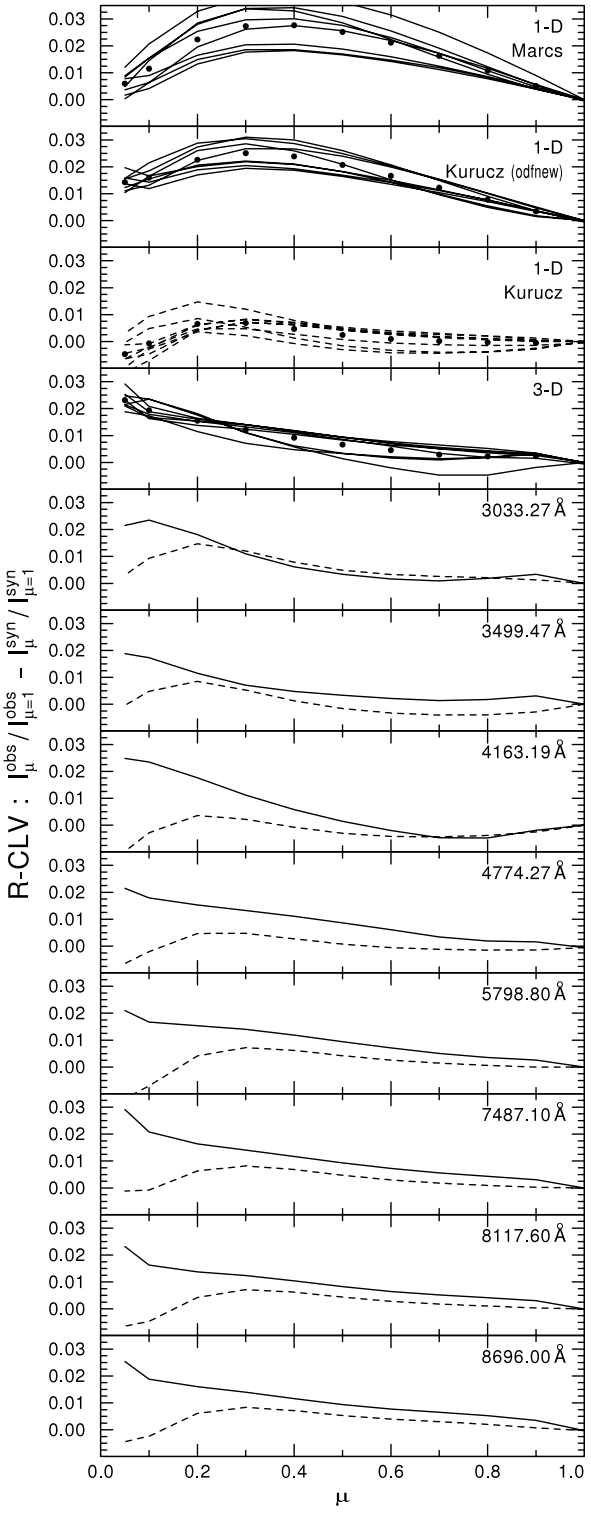

FIG. 2.—Residual CLVs (RCLVs) in the continuum, i.e., the difference of the observed and the synthetic normalized CLVs for the 3D (*solid lines*) and the 1D (*dashed lines*) model. The top four panels show the 1D and 3D data combined, respectively. Average values are indicated by circles. The bottom panels compare separately the data for the six wavelengths under consideration but do not repeat the data from the alternative (ODFNEW) Kurucz and the MARCS model. Positive RCLVs indicate that the temperature drops off too fast in the model atmospheres.

within the 1D data demonstrates vividly the divergence that still persists among different 1D models.

Our reference 1D model (Fig. 2, *third panel*) describes the observed CLVs well down to $\mu \approx 0.5$. Closer to the rim the RCLVs rise to ≈ 0.1 at $\mu = 0.2$ followed by a sharp decline at the rim. In 3D (*fourth panel*) we find on average a linear trend of the RCLVs with μ, showing a maximum residual of $\gtrsim 0.2$ close to the rim.

The investigation of the center-to-limb variation of the continuum is an effective tool to probe the continuum forming region at and above $\tau \approx 1$. Deviations from the observed CLVs indicate that the temperature gradient around $\tau \approx 2/3$ is incorrectly reproduced by the model atmosphere. This can, of course, mean that the gradient in the model is inaccurate, but it can also signal that the opacity used for the construction of the model atmosphere differs significantly from the opacity used for the spectrum synthesis. In that case, the temperature gradient is tested at the wrong depth due to the shift of the τ scales.

Our spectrum calculations suffer from an inconsistency introduced by the fact that the abundance pattern and the opacity cross sections might differ from what was used when the model was constructed. In our reference 1D model, we compensate for the new solar iron abundance ($\epsilon_{\rm Fe}$: 7.63 → 7.45) and interpolate to $\log (Z/Z_\odot) = -0.2$ in the Kurucz model grid (see § 2.4). The 3D model has been constructed based on the Grevesse & Sauval (1998) solar abundances (see Asplund et al. 2000) with $\epsilon_{\rm Fe} = 7.50$ and, to first order, no compensation is necessary. (And the same is true for the other two 1D models considered in Fig. 2.) The changes in carbon and oxygen abundances do not affect the continuum opacities, which are dominated in the optical by H and H^-. Consequently, only metals that contribute to the electron density and therefore to the H^- population (i.e., Fe, Si, and Mg) are relevant.

In order to investigate the impact of changes of the opacity on the center-to-limb variation we have calculated the RCLVs for the 3D and our reference 1D models at 3499.47 Å with two different Fe abundances (±0.3 dex). The purpose of the test is to demonstrate the general effect of opacity variations that can come from different sources, i.e., uncertainties of abundances and uncertainties of bound-free cross sections of all relevant species (not only iron). However, to simplify the procedure we have modified only the abundance of iron which stands for the cumulative effect of all uncertainties. In the example the total opacity is increased by 50% and decreased by 22%, respectively.

Increased opacity, i.e., increased iron abundances, results in large negative residuals, while decreased opacity produces large positive residuals (Fig. 3). Both models are affected in a similar way, but the strength of the effect is slightly smaller for the 3D calculation by about 20% (see Fig. 3, *bottom*). A change in opacity has a significant effect on the CLV, but it does not eliminate the discrepancies.

To estimate the effect of a varied temperature gradient on the RCLVs we have calculated the CLV at 3499.47 Å for two artificially modified 1D models (Fig. 4). The temperature structure around $\tau_{\rm Ross} = 2/3$ is changed such that the gradient in temperature is increased and decreased by 1%, respectively. At $\mu = 0.2$, i.e., the position of the largest discrepancy, the residual of 0.0085 is changed by ≈ 0.0035, i.e., by roughly 1/3, indicating a maximum error of the 1D temperature gradient of about 3%. Again, a simple change does not lead to perfect agreement, especially when more than one frequency is considered.

Finally, we compare the CLV in the continuum for the average ("horizontal" and over time) 3D model with the exact data derived from the radiation transfer in 3D. Figure 5 shows the residual CLVs for both models. The discrepancies with the observations

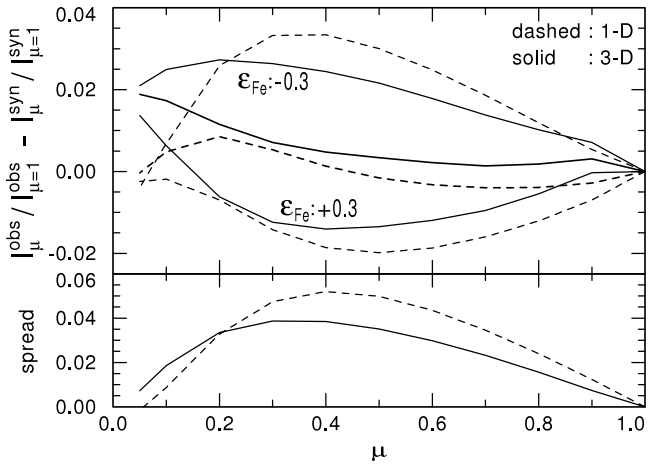

FIG. 3.—*Top*: Residual continuum CLVs at 3499.47 Å derived from the 1D (*dashed lines*) and the 3D model (*solid lines*) with varied Fe abundances of ± 0.3 dex. The unaltered data are highlighted. *Bottom*: Difference of the data in the top panel from the calculation with $\epsilon_{Fe} = \pm 0.3$ dex.

are much more severe for the average 3D model, and it becomes obvious that it does not represent the original 3D time series at all. Although a 1D representation would obviously be highly desirable because it would allow quick calculation of spectra by means of a 1D radiation transfer code, this turns out to be a very poor approximation in this case.

Ayres et al. (2006) have carefully investigated the rotational-vibrational bands of carbon monoxide (CO) in the solar spectrum and have derived oxygen abundances from three models, i.e., the FAL C model (Fontenla et al. 1993), a 1D model that is especially adapted to match the center-to-limb variation of the CO bands (COmosphere), and the averaged 3D time series. In all three cases, temperature fluctuations are accounted for in a so-called 1.5-dimensional approximation, in which profiles from five different temperature structures are averaged. By assuming a C/O ratio of 0.5, Ayres et al. (2006) derive a high oxygen abundance close to the "old" value from Grevesse & Sauval (1998) from both the FAL C and the COmosphere model, discarding the low oxygen abundance derived from the mean 3D model because its temperature gradient is too steep around $\tau_{0.5\ \mu m} \approx 1$ and fails to reproduce the observed center-to-limb variations.

Our current study documents that the mean 3D model is not a valid approximation of the 3D time series, and therefore its performance cannot be taken as indicative of the performance of the 3D model, and in particular of its temperature profile. We find that the center-to-limb variation of the continuum predicted by the 3D simulation matches the observations reasonably well

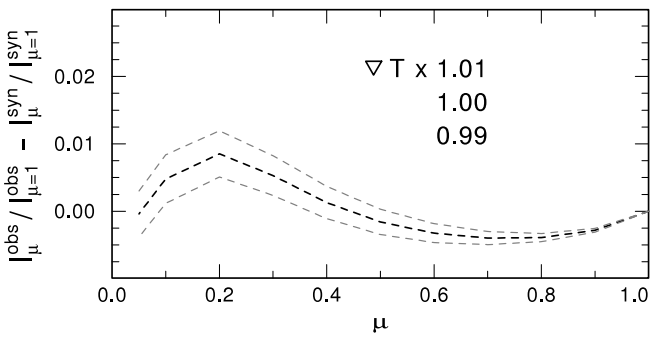

FIG. 4.—Residual continuum CLVs at 3499.47 Å from the 1D model with modified temperature fields. The temperature gradient at $\tau \approx 2/3$ is changed by +1% (*top curve*) and −1% (*bottom curve*). The unaltered data are highlighted.

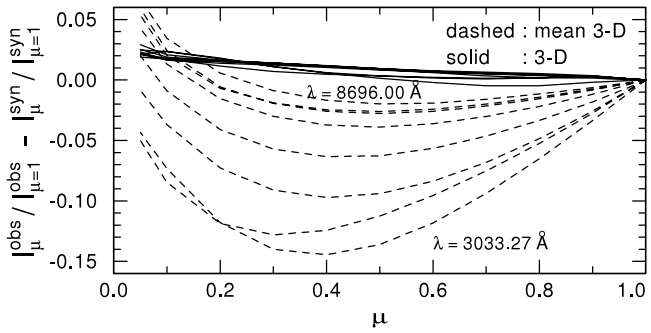

FIG. 5.—Residual CLVs in the continuum, i.e., the difference of the observed and the synthetic normalized CLVs for the 3D model (*solid lines*) and its 1D approximation (*dashed lines*). In comparison, the approximation in 1D, i.e., the "horizontal" time average of the 3D model, fails to reproduce the observed center-to-limb variation at all. The maximum absolute residual is up to 5 times larger, i.e., −0.15 (1D) vs. 0.03 (3D).

(i.e., similar to the best 1D model in our study). The results by Scott et al., based on 3D radiative transfer on the same hydrodynamical simulations used here, indicate that the observed CO rovibrational lines are consistent with the low oxygen and carbon abundances. Our results show that there is no reason to distrust the 3D-based abundances on the basis of the simulations having a wrong thermal profile.

3.2. *Lines*

We study the center-to-limb variation of a number of lines by comparing observations of the quiet Sun taken at six different heliocentric angles to synthetic profiles derived from 3D and 1D models. The observations are described in detail by Allende Prieto et al. (2004) and were previously used for the investigation of inelastic collisions with neutral hydrogen on oxygen lines formed under non-LTE conditions.[6] The observations cover eight spectral regions obtained at six different positions on the Sun. The first five slit positions are centered at heliocentric angles of $\mu \equiv \cos\theta = 1.00$, 0.97, 0.87, 0.71, and 0.50. The last position varies between $\mu = 0.26$ and 0.17 for different wavelength regions. This translates to distances of the slit center from the limb of the Sun of 16.00′, 12.11′, 8.11′, 4.74′, 2.14′, 0.54′, and 0.24′, assuming a diameter of the Sun of 31.99′. For both of these last positions the slit extends beyond the solar disk and the center of the illuminated slit corresponds to $\mu = 0.34$ and 0.31 (0.96′ and 0.78′).

We have calculated a variety of line profiles for the six positions defined by the center (in μ) of the illuminated slit. Although the slit length, 160″, is rather large, test calculations show that averaging the spectrum from six discrete μ-angles spanning the slit length gives virtually the same equivalent width as the spectrum from the central μ. For $\mu = 0.5$, the second-last angle, the difference amounts to a marginal change of the log (gf) value of about 0.01. To further reduce the computational burden we have derived the average 3D profiles from calculations taking only 50 (every other) of the 99 snapshots into account.

We have selected 10 seemingly unblended lines from five different neutral ions. The list of lines is compiled in Table 1. The log (gf) values for most lines were adopted from laboratory measurements at Oxford (e.g., Blackwell et al. 1995 and references therein) and by O'Brian et al. (1991).

We are interested in how synthetic line profiles deviate from observations as a function of the position angle μ for two reasons. First of all, any clear trend with μ would reveal shortcomings of the theoretical model atmospheres similar to our findings presented

[6] Data are available at http://hebe.as.utexas.edu/izana.

TABLE 1
LINES

Line	R'[a]	max (θ) (deg)	log (gf)	log $\Gamma_{\rm Rad}$[b]	log $\Gamma_{\rm Stark}$[c]	log $\Gamma_{\rm VdW}$[d]
Fe I λ5242.5	56000	75	−0.970	7.76	−6.33	−7.58
Fe I λ5243.8	56000	75	−1.050	8.32	−4.61	−7.22
Fe I λ5247.0	56000	75	−4.946	3.89	−6.33	−7.82
Fe I λ6170.5[e]	77000	80	−0.380	8.24	−5.59	−7.12
Fe I λ6200.3[f]	206000	75	−2.437	8.01	−6.11	−7.59
Fe I λ7583.8	176000	80	−1.880	8.01	−6.33	−7.57
Cr I λ5247.6	56000	75	−1.627	7.72	−6.12	−7.62
Ni I λ5248.4	56000	75	−2.426	7.92	−4.64	−7.76
Si I λ6125.0	77000	80	−0.930	...[g]	...	...
Ti I λ6126.2	77000	80	−1.425	6.85	−6.35	−7.73

[a] See Allende Prieto et al. (2004); R' is the resolving power measured relative to the FTS ($R_{\rm FTS} \approx 400,000$) spectrum at the center-disk provided by Brault & Neckel (1987; see also Neckel 1994).
[b] $\Gamma = \gamma$, where γ is the damping constant (FWHM of a Lorentzian profile, see, e.g., eq. [11.13] in Gray 1992), in rads per second. Here $\epsilon_{\rm X} = N_{\rm X}/N_{\rm H} \times 10^{12}$, where $N_{\rm X}$ represents the number density of nuclei of element X.
[c] $\Gamma = \gamma/N_e$, where N_e indicates the number density of electrons at a temperature of 10,000 K (cgs units).
[d] $\Gamma = \gamma/N_{\rm H}$, where $N_{\rm H}$ is the hydrogen number density at a temperature of 10,000 K.
[e] Noticeable blend at +5 km s^{-1}.
[f] Marginal blend at +5 km s^{-1}.
[g] Approximate values were adopted for this line; see, e.g., Gray (1992).

in § 3.1. But, arguably, even more relevant is the fact that any significant deviation (scatter) would add to the error bar attached to a line-based abundance determination.

In our present study we compare synthetic line profiles from 3D and 1D models with the observations. Due to the inherent deficiencies of the latter models, e.g., no velocity fields and correspondingly narrow and symmetric line profiles, we focus on line strengths and compare observed and synthetic line equivalent widths, rather than comparing the line profiles in detail. To be able to detect weak deviations, we have devised the following strategy. We have identified wavelength intervals around each line under consideration for the contribution to the line equivalent widths and have calculated series of synthetic line profiles in 1D and 3D with varied log (gf) values that encircle the observations with respect to their equivalent widths. That allowed us to determine by interpolation the log (gf) value required to match the observed line equivalent widths separately for each position angle ("best fit"). To keep interpolation errors at a marginal level we have applied a small step of $\Delta[\log(gf)] = 0.05$ for these series of calculations. A simple normalization scheme has been applied. All profiles have been divided by the maximum intensity found in the vicinity of the line center (within ± 15 km s^{-1}). We convolved the synthetic profiles with a Gaussian to mimic the instrumental profile (see Table 1). An additional Gaussian broadening is applied to the line profiles from the 1D calculation to account for macroturbulence; this value was adjusted for each line in order to reproduce the line profiles observed at the disk center.

Finally, we have translated variations of line strength into variations of abundance; i.e., we have identified $\Delta \log(gf) = \Delta \log \epsilon$. This approximation is valid because the impact of slight changes in a metal abundance on the continuum in the optical is marginal. Note that it is not the intent of this study to derive metal abundances from individual lines. Such an endeavor would require a more careful consideration regarding line blends, continuum normalization, and non-LTE effects.

All calculations described in this section are single-line calculations; i.e., no blends with atomic or molecular lines are accounted for. The observations did not have information on the absolute wavelength scale (see Allende Prieto et al. 2004), but that is not important for our purposes, and the velocity scales in Figures 6 and 7 are relative to the center of the line profiles. The individual synthetic profiles were convolved with a Gaussian profile to match the observed profiles (see Table 1). We were generally able to achieve a better fit of the observations when slightly less broadening was applied to the 3D profiles (0.3% in case of Fe I λ5242.5). Since we know from previous investigations that the theoretical profiles derived from 3D hydro-models match the observations well, we argue that the resolution of the observations is actually slightly higher than estimated by Allende Prieto et al. (2004). An alternative explanation would be that the amplitude of the velocity field in the models is too high. Such a finding, if confirmed, deserves a deeper investigation but is beyond the scope of this study since line equivalent widths are only marginally (if at all) affected.

We introduce the lines under consideration by showing the observed center-disk line profiles and the "best fits" derived from the 3D calculations of the six Fe I lines and the four lines from other ions in Figures 6 and 7, respectively. In Figure 8 we exemplify the fitting process by means of the Fe I line at 5242.5 Å and show the relative difference between the observation and a variety of model calculations for all six angles under consideration. The "best fit" log (gf) values are derived by interpolation to match the observed equivalent widths from the spectral region around the line profile.

We have obtained "best fits" for all 10 lines (see Table 1) and present the log (gf) values as a function of μ in Figure 9. Be reminded that the aim of this study is not the measurement of absolute abundances: we focus on relative numbers and normalize our results with respect to the disk center ($\mu = 1$).

For improved readability we subdivide our findings presented in Figure 9 into four distinct groups: iron lines, non-iron lines, 1D calculations, and 3D calculations, respectively. We focus our discussion on the first five data points because we have some indications that the data obtained for the shallowest angle are less trustworthy than the data from the other angles: (1) the relative contribution of scattered light was estimated from the comparison of the center-disk spectrum with the Fourier transform

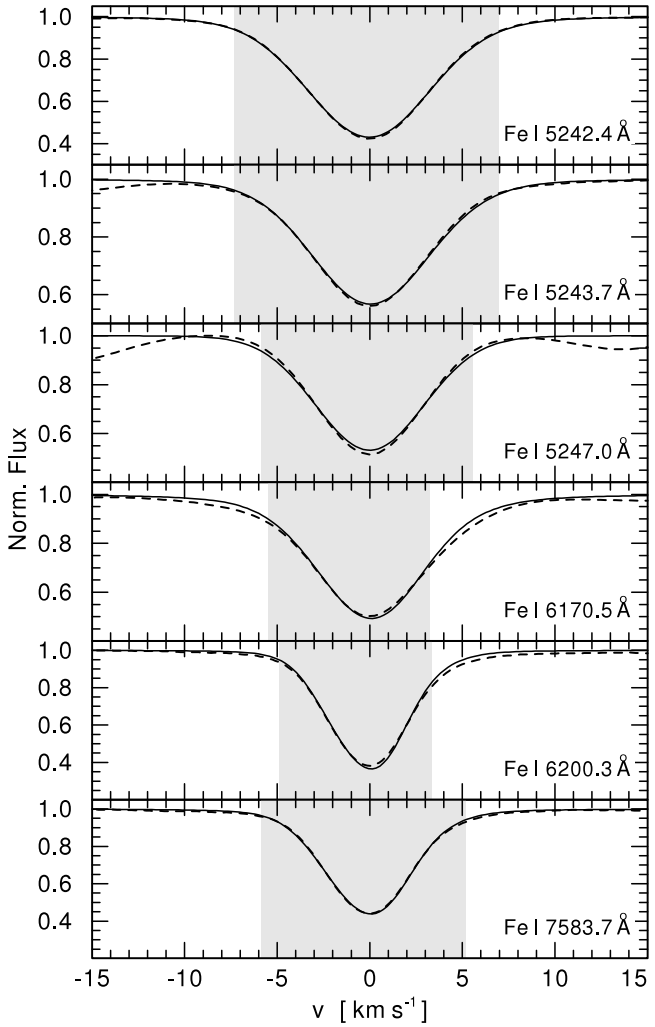

FIG. 6.—Iron lines under consideration. Observed (*dashed lines*) and synthetic (*solid lines*) profiles are shown for the disk center. The gray areas mark the velocity ranges used for the calculation of the line equivalent widths. The zero of the velocity scale refers always to the center of the observed line profile, as approximately determined by polynomial fitting. The $\log(gf)$ values are modified to match the observed line equivalent widths. For most lines the profiles match well. However, the synthetic profile of the line at 5247.0 Å seems to be broader than the observed profile. The line at 6200.3 Å is marginally blended around +5 km s^{-1}. The line at 6170.5 Å is noticeably blended around +5 km s^{-1}. For both lines the wavelength interval is decreased accordingly.

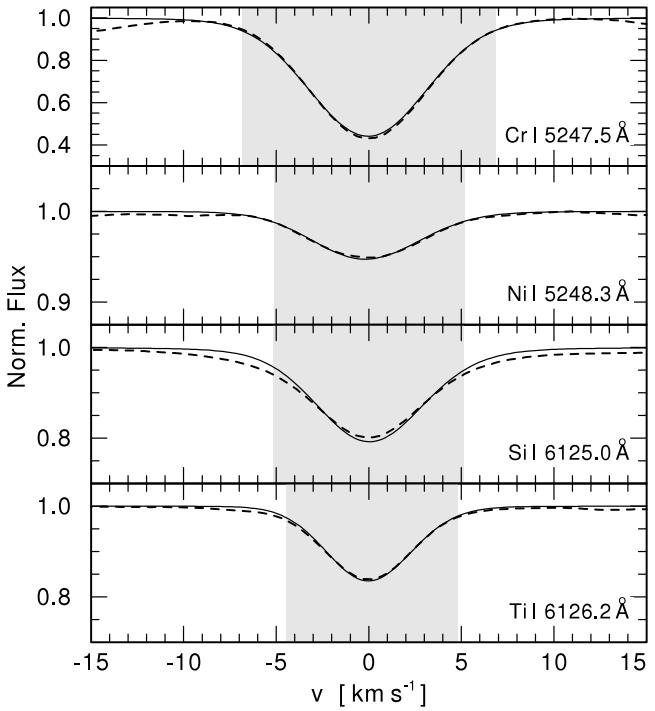

FIG. 7.—Non-iron lines under consideration. Observed (*dashed lines*) and synthetic (*solid lines*) profiles are shown for the center-disk. The gray areas mark the wavelength ranges used for the calculation of the line equivalent widths. The $\log(gf)$ values are modified to match the observed line equivalent widths. For most lines the profiles match well. However, the synthetic profile of the Si I line at 6125.0 Å is noticeably narrower than observed.

spectrum (FTS) taken from Brault & Neckel (1987; see also Neckel 1994) and the outermost position was the only one for which the entire slit was not illuminated; (2) for all 10 lines the fit of the line profiles for this particular angle is the worst (see Fig. 8); and (3) the scatter in our data presented in Figure 9 is the largest for this angle. Fortunately, the flux integration is naturally biased toward the center of the disk.

We find this systematic behavior for all six iron lines: $\Delta \log \epsilon$ in 1D is larger than or equal to $\Delta \log \epsilon$ in 3D, for all but one line (Fe I λ6170.5) $\Delta \log \epsilon$ is positive or zero for the 1D calculations, and $\Delta \log \epsilon$ is negative or zero for all 3D calculations. The Fe I line at 6170.5 Å stands out in both comparisons. In 1D it is the only line with a negative $\Delta \log \epsilon$, and in 3D it shows the by far largest negative $\Delta \log \epsilon$. This might be related to the noticeable line blend (see Fig. 6).

The iron lines calculated in 3D indicate a uniform trend of decreased $\log(gf)$ values with increased distance from the center-disk. The average decrease at $\mu = 0.5$ for this group is -0.015 (Fe I λ6170.5 excluded). From the 1D calculations we derive the opposite trend for the same group of lines and obtain an average of 0.103. Obviously, the 3D model performs significantly better than the 1D reference model regarding the center-to-limb variation of Fe I lines, even when equivalent widths, and not line asymmetries or shifts, are considered.

For these five Fe I lines we obtain an average difference (1D vs. 3D) of 0.12 at $\mu = 0.5$. To estimate the impact on abundance determinations based on solar fluxes we apply a three-point Gaussian integration, neglecting the shallowest angle at $\mu = 0.11$ (which has, by far, the smallest integration weight) for which we have no data, and assuming that the good agreement between the 1D and the 3D calculations for the central ray implies an equally good agreement for the first angle at $\mu = 0.89$. These estimates lead to an abundance correction of approximately 0.06 dex between 1D and 3D models due to their different center-to-limb variation. Asplund et al. (2000) found a similar correction from the comparison of 1D and 3D line profiles at the disk center.

For the four non-iron lines we find a uniform trend of increasing $\log(gf)$ values with decreasing μ for both the 1D and the 3D data set. The systematic behavior is similar to what we find for the iron lines, but now the performance of the 1D and 3D models is similar, and the offsets are in the same sense: larger abundances would be found toward the limb for both models.

4. CONCLUSION

The photosphere of cool stars and the Sun can be described by stellar atmospheres in 1D and 3D. Since the 3D models add more realistic physics, i.e., the hydrodynamic description of the gas, they can be seen truly as an advancement over the 1D models. However, this refinement increases the computational effort by many orders of magnitude. In fact, the computational workload

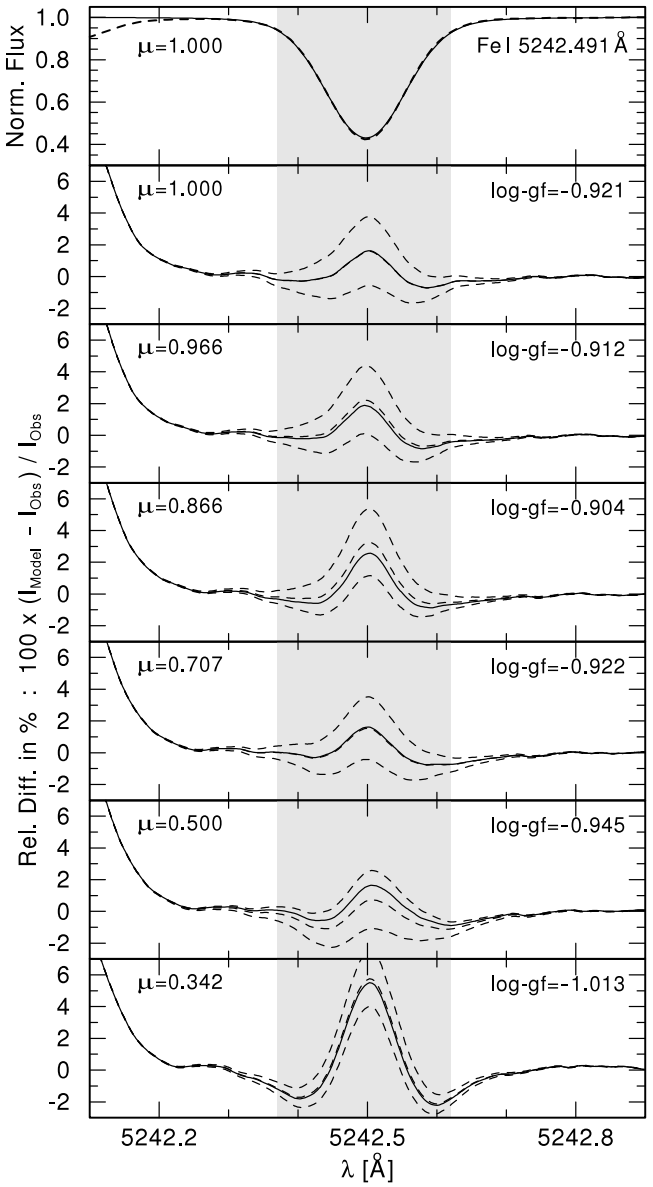

FIG. 8.—Fit of the Fe I line at 5242.5 Å with synthetic profiles derived from the 3D hydro-model. The top panel shows the normalized profiles of the center-disk observation (*dashed line*) and the "best fit" synthetic profile (*solid line*). The bottom six panels show the relative difference of the observation and three synthetic profiles (*dashed lines*), i.e., three different $\log(gf)$ values for the six angles under consideration. The equivalent widths of the "best fits" (*solid lines*) match the observed equivalent widths. The wavelength range considered for the equivalent width is highlighted in gray. The fit improves when a slightly higher resolution (by ≈0.3%) is assumed. However, line equivalent widths are only marginally affected.

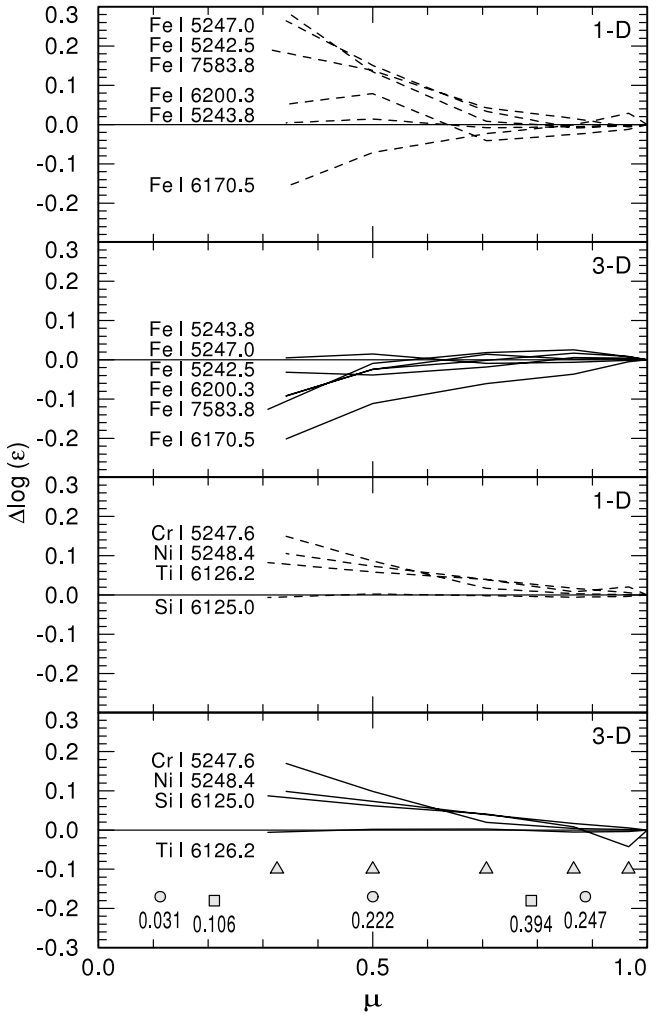

FIG. 9.—Relative abundance variations with respect to the center-disk ($\mu = 1$) from the 1D (*dashed lines*) and 3D calculations (*solid lines*). The top two panels show the six Fe I lines, and the bottom two panels show the four lines from the other elements. Line designations are given in the left part of the plot. In the second panel from the top, the curves for the iron lines at 5242.5 and 6200.3 Å overlap with each other for the two positions closest to the limb. The bottom panel also indicates the six μ-angles of the observations (*triangles*, $\mu = 1$ not shown, shallowest angle varies slightly) and the μ-angles used in a two-point (*squares*) and a three-point (*circles*) Gaussian flux integration and their respective integration weights ($\sum w_\mu = 0.5$).

becomes so demanding that the description of the radiation field has to be cut back to very few frequencies, i.e., to a rudimentary level that had been surpassed by 1D models over 30 years ago. Overall we are left with the astonishing situation that a stellar photosphere can be modeled either by an accurate description of the radiation field with the help of a makeshift account of stellar convection (mixing-length theory) or by an accurate description of the hydrodynamic properties augmented by a rudimentary account of the radiation field.

It is evident that individual line profiles can be described to a much higher degree and without any artificial micro- or macroturbulence by the 3D hydrodynamical models, as the simulations account for Doppler shifts from differential motions within the atmosphere. We know from detailed investigations of line profiles that the velocity field is described quite accurately and that the residuals of the fittings to line profiles are reduced by about a factor of 10. However, it is not obvious how the 3D models compare to their 1D counterparts when it comes to reproducing spectral energy distributions and line strengths.

We study the solar center-to-limb variation for several lines and continua, to probe the temperature structure of 3D models. The work is facilitated by the new code ASSεT, which allows for the fast and accurate calculation of spectra from 3D structures. In comparison to other programs (e.g., Asplund et al. 2000; Ludwig & Steffen 2008), the attributes of the new code are a greater versatility, i.e., the ability to handle arbitrarily complicated line blends on top of nonconstant background opacities, higher accuracy due to the proper incorporation of scattering and improved (higher order) interpolation schemes, and a higher computational speed when the same simplifications are adopted.

In our study we find that regarding center-to-limb variations, the overall shortcomings of the 3D model are roughly comparable

to the shortcomings of the 1D models. First, we conclude from the investigation of the continuum layers that the models' temperature gradient is too steep around $\tau \approx 2/3$. This behavior is more pronounced for the 3D model which shows a drop in intensity (with μ) that is about twice the size of the drop displayed by our reference 1D model, but at the same time smaller than the discrepancies found for two other (newer!) 1D structures. Second, the line profiles for different position angles on the Sun cannot be reproduced by a single abundance. For Fe I lines, the abundance variation between the disk center and $\mu = 0.5$ is about 0.1 dex for our reference 1D model but only 0.015 dex (and with the opposite sign) for the 3D simulations, albeit the calculations for lines of other neutral species suggest a more balanced outcome.

Overall we conclude that the 1D and 3D models match the observed temperature structure to a similar degree of accuracy. This is somewhat surprising, but it might be that the improved description of the convective energy transport is offset by deficiencies introduced by the poor radiation transfer. Once new hydrodynamical models based on an upgraded radiation transfer scheme (i.e., more frequencies and angles, better frequency binning) become available in the near future, we will be able to test this hypothesis. It will become clear whether focusing on refining the radiation transfer will be enough to achieve better agreement with observations, or whether the hydrodynamics needs to be improved as well.

We thank M. Asplund for providing us with the 3D hydrodynamical simulation and the 1D MARCS model, and M. Bautista, I. Hubeny, and S. Nahar for crucial assistance in computing opacities. We extend our thanks to the late John Bahcall, Andy Davis, and Marc Pinsonneault for their interest on our tests of the solar simulations, which enhanced our motivation to carry out this work. Continuing support from NSF (AST 00-86321), NASA (NAG5-13057 and NAG5-13147), and the Welch Foundation of Houston is greatly appreciated.

REFERENCES

Allende Prieto, C. 2008, in ASP Conf. Ser. 384, 14th Cambridge Workshop on Cool Stars, Stellar Systems, and the Sun, ed. G. van Belle (San Francisco: ASP), 39
Allende Prieto, C., Asplund, M., & Bendicho, P. F. 2004, A&A, 423, 1109
Allende Prieto, C., Beers, T. C., Wilhelm, R., Newberg, H. J., Rockosi, C. M., Yanny, B., & Lee, Y. S. 2006, ApJ, 636, 804
Allende Prieto, C., Lambert, D. L., & Asplund, M. 2001, ApJ, 556, L63
———. 2002, ApJ, 567, 544
Allende Prieto, C., Lambert, D. L., Hubeny, I., & Lanz, T. 2003, ApJS, 147, 363
Asplund, M., Grevesse, N., & Sauval, A. J. 2005a, in ASP Conf. Ser. 336, Cosmic Abundances as Records of Stellar Evolution and Nucleosynthesis, ed. T. G. Barnes, III, & F. N. Bash (San Francisco: ASP), 25
Asplund, M., Grevesse, N., Sauval, A. J., Allende Prieto, C., & Blomme, R. 2005b, A&A, 431, 693
Asplund, M., Grevesse, N., Sauval, A. J., Allende Prieto, C., & Kiselman, D. 2004, A&A, 417, 751
Asplund, M., Nordlund, Å., Trampedach, R., Allende Prieto, C., & Stein, R. F. 2000, A&A, 359, 729
Asplund, M., Nordlund, Å., Trampedach, R., & Stein, R. F. 1999, A&A, 346, L17
Auer, L. 2003, in ASP Conf. Ser. 288, Stellar Atmosphere Modeling, ed. I. Hubeny, D. Mihalas, & K. Werner (San Francisco: ASP), 3
Ayres, T. R., Plymate, C., & Keller, C. U. 2006, ApJS, 165, 618
Bahcall, J. N., Basu, S., Pinsonneault, M., & Serenelli, A. M. 2005, ApJ, 618, 1049
Barklem, P. S., Piskunov, N., & O'Mara, B. J. 2000, A&AS, 142, 467
Bautista, M. A. 1997, A&AS, 122, 167
Blackwell, D. E., Lynas-Gray, A. E., & Smith, G. 1995, A&A, 296, 217
Brault, J., & Neckel, H. 1987, Spectral Atlas of Solar Absolute Disk-Averaged and Disk-Center Intensity from 3290 to 12510 (tape copy included as part of the KIS IDL library)
Delahaye, F., & Pinsonneault, M. H. 2006, ApJ, 649, 529
Elste, G., & Gilliam, L. 2007, Sol. Phys., 240, 9
Fontenla, J. M., Avrett, E. H., & Loeser, R. 1993, ApJ, 406, 319
Fontenla, J. M., Balasubramaniam, K. S., & Harder, J. 2007, ApJ, 667, 1243
Gray, D. F. 1992, The Observation and Analysis of Stellar Photospheres, (2nd ed.; Cambridge: Cambridge Univ. Press)
Grevesse, N., & Sauval, A. J. 1998, Space Sci. Rev., 85, 161
Hubeny, I., & Lanz, T. 1995, SYNSPEC—a Users's Guide (College Park: Univ. Maryland), http://nova.astro.umd.edu/Tlusty2002/pdf/syn43guide.pdf
Kurucz, R. 1993, CD-ROM 13, ATLAS9 Stellar Atmosphere Programs and 2 km/s Grid (Cambridge: SAO)
Kurucz, R. L., Furenlid, I., Brault, J., & Testerman, L. 1984, National Solar Observatory Atlas (Sunspot: NSO)
Lin, C.-H., Antia, H. M., & Basu, S. 2007, ApJ, 668, 603
Ludwig, H.-G., & Steffen, M. 2008, in Precision Spectroscopy in Astrophysics, ed. L. Pasquini et al. (Berlin: Springer), 133
Nahar, S. N. 1995, A&A, 293, 967
Neckel, H. 1994, in IAU Colloq. 143, The Sun as a Variable Star, ed. J. M. Pap et al. (Cambridge: Cambridge Univ. Press), 37
———. 2003, Sol. Phys., 212, 239
———. 2005, Sol. Phys., 229, 13
Neckel, H., & Labs, D. 1994, Sol. Phys., 153, 91
Nordlund, Å., & Stein, R. F. 1990, Comput. Phys. Commun., 59, 119
O'Brian, T. R., Wickliffe, M. E., Lawler, J. E., Whaling, J. W., & Brault, W. 1991, J. Opt. Soc. Am. B, 8, 1185
Olson, G. L., & Kunasz, P. B. 1987, J. Quant. Spectrosc. Radiat. Transfer, 38, 325
Petro, D. L., Foukal, P. V., Rosen, W. A., Kurucz, R. L., & Pierce, A. K. 1984, ApJ, 283, 426
Scott, P. C., Asplund, M., Grevesse, N., & Sauval, A. J. 2006, A&A, 456, 675
Socas-Navarro, H., & Norton, A. A. 2007, ApJ, 660, L153
Stein, & R. F., Nordlund, Å. 1989, ApJ, 342, L95